Electronic Supplementary Information (ESI) Materials Horizons.

Electronic Supplementary Information
Dramatic Enhancement of Nonlinear Optical Signals in Distinct Two-Dimensional Materials

Shu-Hsien Chen[a], Wei-Hsuan Kung[a], Yu-Chen Chen[a], Yu-Ming Chang[c], Wei-Liang Chen[c], and Hsuen-Li Chen[a,b*]

S.-H. Chen[a], W.-H. Kung[a], Y.-C. Chen[a], Y.-M. Chang[c], W.-L. Chen[c], and H.-L. Chen[a,b*]

[a] Department of Materials Science and Engineering, National Taiwan University, No. 1, Sec. 4, Roosevelt Road, Taipei, 10617, Taiwan.

[b] Center of Atomic Initiative for New Materials, National Taiwan University, No. 1, Sec. 4, Roosevelt Road, Taipei, 10617, Taiwan.

[c] Center for Condensed Matter Sciences, National Taiwan University, No. 1, Sec. 4, Roosevelt Road, Taipei, 10617, Taiwan.

*Corresponding author E-mail: hsuenlichen@ntu.edu.tw

Supplementary Information Note S1. Optimization of the Surface Electric Field

According to the structure optimization results, a 50 nm Al layer is sufficient to approximate a perfect reflective layer. Furthermore, the air-gap depth of 125 nm was determined based on a parametric sweep using FDTD simulations, in which the gap depth was varied from 50 nm to 1000 nm with a 5 nm step. **Figure S1** shows the field distributions for four representative depths, corresponding to the top-four condition in which constructive interference of both the incident and emitted light maximizes the electric field, resulting in the highest SHG and Raman enhancement. As shown in **Table S1**, the surface electric-field enhancement of the suspended 2D material was calculated for each gap thickness at the SHG excitation wavelength (800 nm) and the SHG emission wavelength (400 nm), with 125 nm identified as the optimal depth.

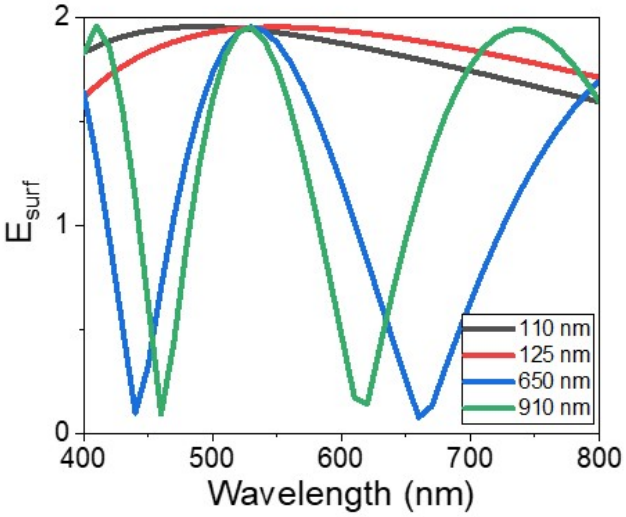

Figure S1 The surface electric field on various depths of air-gap nanocavity over the wavelength range of 400–800 nm.

Table S1 The enhancement of E_{surf}^{2} and E_{surf}^{4} under SHG emission wavelength (400 nm) and excitation wavelength (800 nm).

Depth of air-gap nanocavity	E_{surf}^{2} **(400 nm)**	E_{surf}^{4} **(800 nm)**	E_{surf}^{2} **(400 nm) x** E_{surf}^{4} **(800 nm)**
110 nm	3.36	6.50	21.85
125 nm	2.62	8.63	22.62
650 nm	2.70	8.27	22.33
910 nm	3.36	6.50	21.85

Moreover, to provide direct visualization of the enhanced electric field, we have performed FDTD simulations of the spatial electric field distribution of a 2D material suspended in a 125 nm air gap nanocavity at wavelengths of 400 nm, 532 nm, and 800 nm. As shown in **Figure S2**, these field maps clearly illustrate the spatial enhancement of the electric field of the suspended 2D materials.

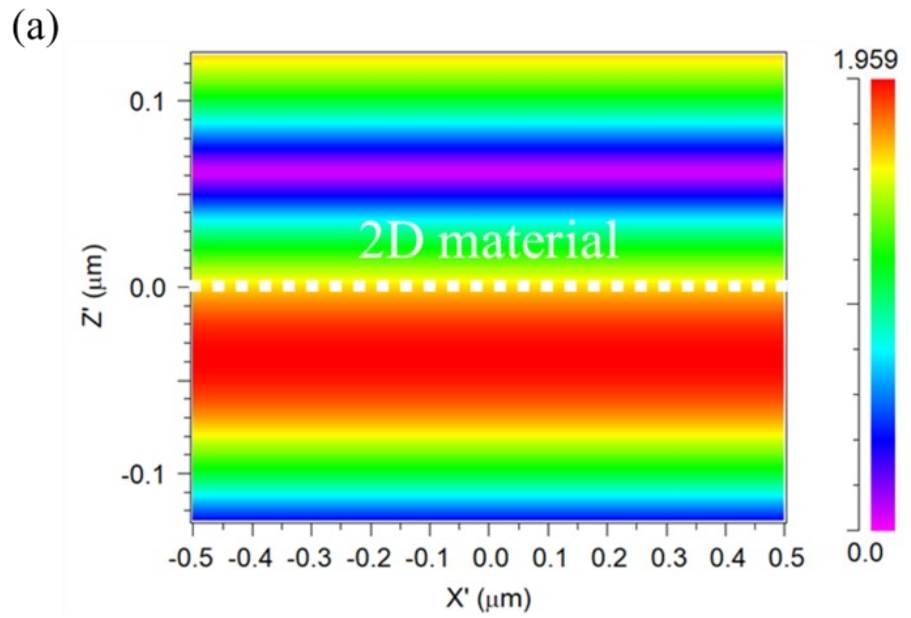

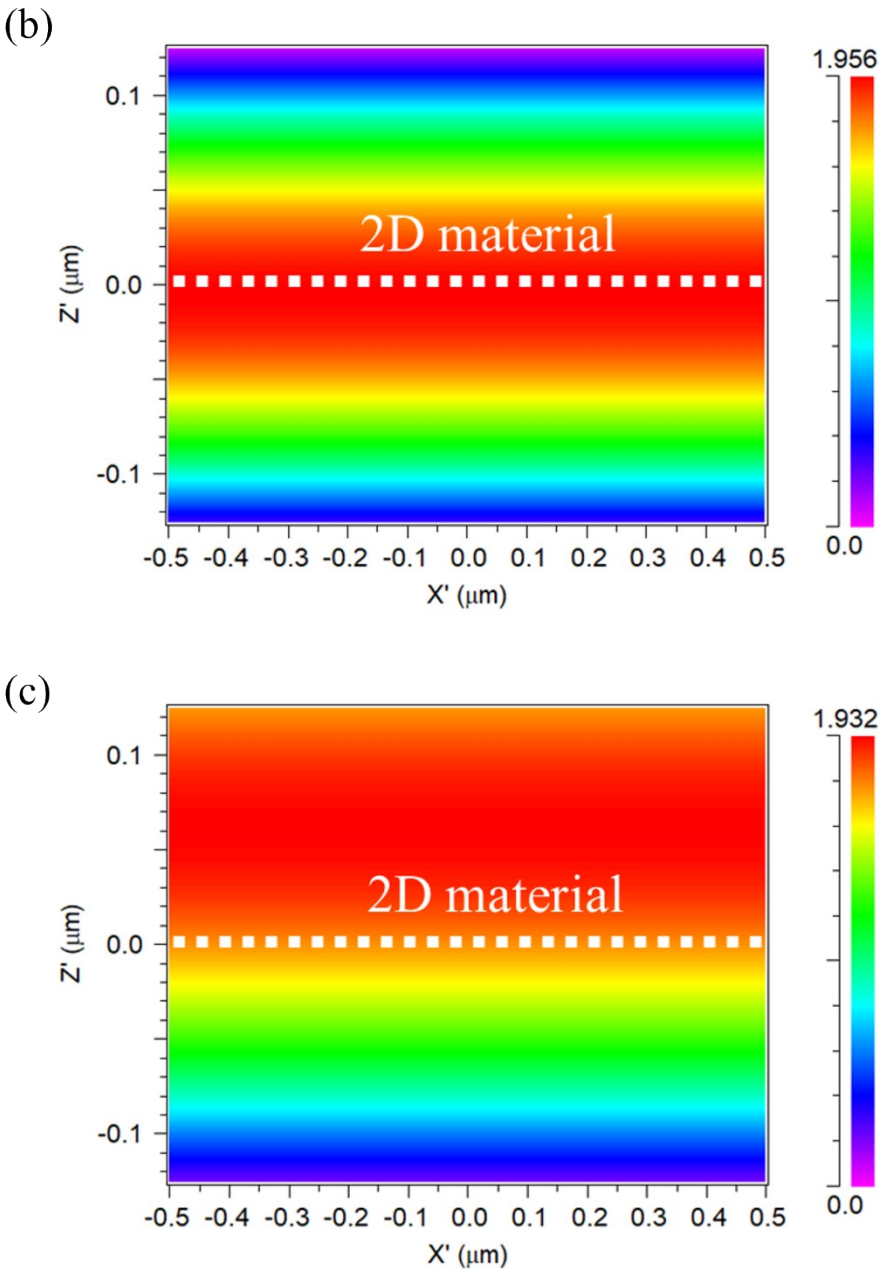

Figure S2 The electric field distribution of a 2D material suspended in a 125 nm air gap nanocavity at wavelengths of (a) 400 nm, (b) 532 nm, and (c) 800 nm, respectively.

Supplementary Information Note S2. Optical admittance analysis

In this study, the depth of the air-gap nanocavity is optimized to maximize the surface electric field. According to the transfer matrix formalism, the relationship between the optical admittance of a multilayer thin-film system and the amplitude of the surface electric field has been established in previous studies and can be expressed as:[1]

$$E_{surface} = \sqrt{\frac{4}{(\alpha+1)^2+\beta^2}} \qquad (1)$$

where α and β represent the real and imaginary parts of the optical admittance y, respectively. When both α and β approach zero, constructive interference occurs at the surface, leading to a maximized surface electric-field amplitude of 2. To quantitatively evaluate the enhancement capability of the air-gap-based cavity, we calculated the optical admittance of a cavity consisting of an air-gap-based cavity on a planar Al substrate at excitation wavelengths of 400, 532, and 800 nm. **Figure S3** presents the evolution of the optical admittance loci as a function of air-gap depth. With increasing air-gap thickness, the admittance trajectories progressively shift toward a regime where both the real and imaginary components are suppressed. This trend indicates that the air-gap cavity can be tuned toward the optimal interference condition. Notably, an air-gap depth of 125 nm enables effective surface electric-field enhancement simultaneously at 400, 532, and 800 nm.

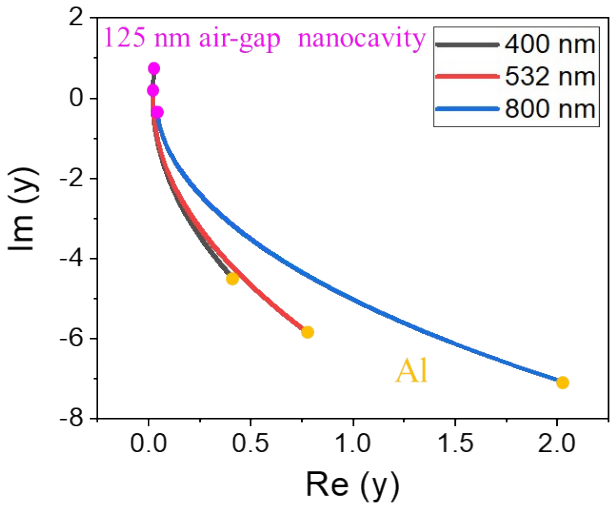

Figure S3 Calculated optical admittance loci of cavities comprising an air-gap cavity of varying depth on Al.

Supplementary Information Note S3. Surface electric field enhancement of 2D MoS_2

To estimate surface electric field enhancement of 2D MoS_2 on various substrates, we analyzed the electric field intensity enhancement for both SHG excitation (800 nm) and emission (400 nm), as well as for Raman excitation (532 nm). The surface electric field (E_{surf}) of the 2D MoS_2 suspended was evaluated using 3D finite-difference time-domain (3D-FDTD) simulations.

Table S2. (a) The enhancement of E_{surf}^{2} and E_{surf}^{4} under SHG emission wavelength (400 nm) and excitation wavelength (800 nm), respectively. (b) The enhancement of E_{surf}^{4} under Raman scattering (532 nm).

(a)

Substrate	E_{surf}^{2} (400 nm)	E_{surf}^{4} (800 nm)
Air-gap nanocavity	1.65	10.22
Si	0.084	0.033
300 nm SiO_2/Si	0.57	0.077
Al	0.18	0.0030

(b)

Substrate	E_{surf}^{4} (532 nm)
Air-gap nanocavity	7.75
Si	0.021
300 nm SiO_2/Si	1.07
Al	0.0123

Supplementary Information Note S4. Scanning electron microscope images of the air-gap cavity

The top view reveals that the cavity structure features square holes with a side length of 3 μm and a periodicity of 6 μm, arranged in a hexagonal pattern. The cross-sectional image reveals that the trenches have an average depth of approximately 125 nm, while the Al film has a thickness of around 50 nm.

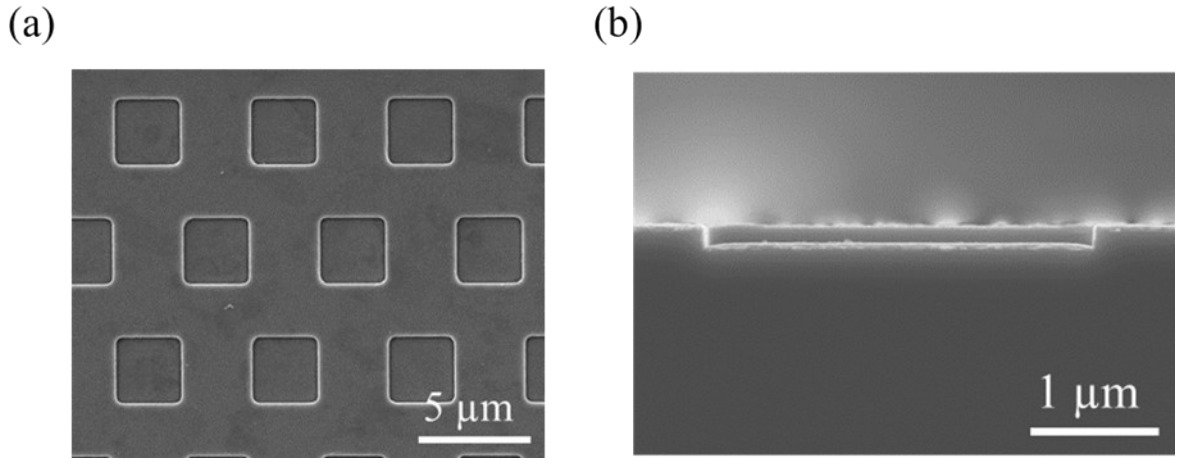

Figure S4. (a) Top view and (b) cross-sectional scanning electron microscope images of the air-gap nanocavity.

Supplementary Information Note S5. Thickness of MoS_2 flakes

Thickness of MoS_2 flakes was confirmed through atomic force microscopy (AFM).

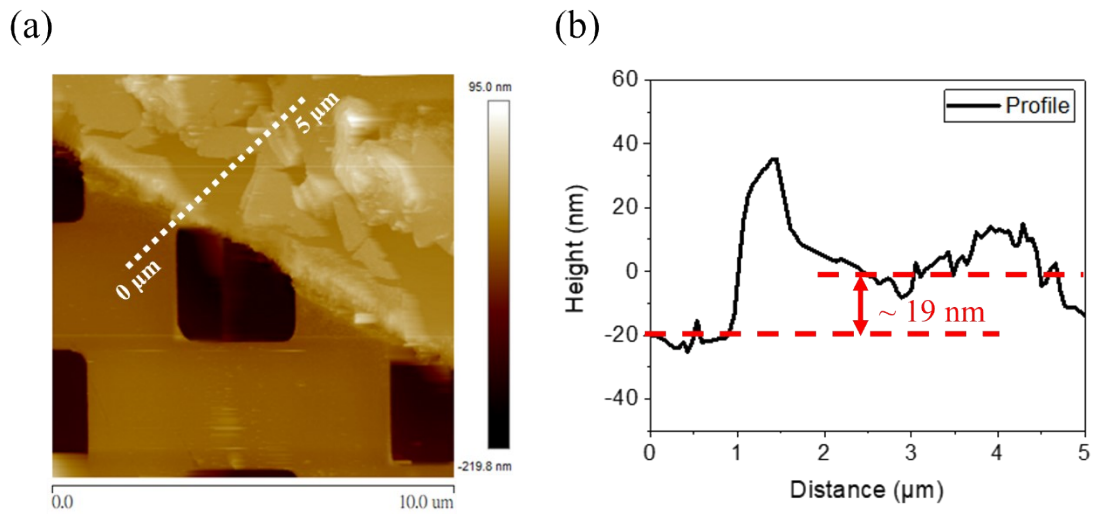

Figure S5. (a) AFM imaging of exfoliated MoS_2 flakes on an air-gap nanocavity, the white-dashed line represents height measurement. (b) Cross-sectional height profile obtained. The thickness of the MoS_2 flake in (a) is approximately 19 nm.

Supplementary Information Note S6. Repeatability tests

In total, five independently prepared samples were measured. For each sample, SHG signals were collected at five different positions in both the supported and suspended regions. The spectra shown in **Figures S6（a) and S6(b)** correspond to the averaged SHG spectra from five positions for each sample. Therefore, the five curves shown in each panel represent five independent samples, with each curve being the average over five measurement positions.

Figure S6(c) presents a statistical comparison of the SHG intensities between the supported and suspended configurations. The data are shown as mean values with error bars representing the standard deviation, calculated from all measurements (n = 25) for each configuration. The suspended MoS_2 consistently exhibits SHG intensities that are several orders of magnitude higher than those of the supported MoS_2, confirming that the reported enhancement factors are highly reproducible.

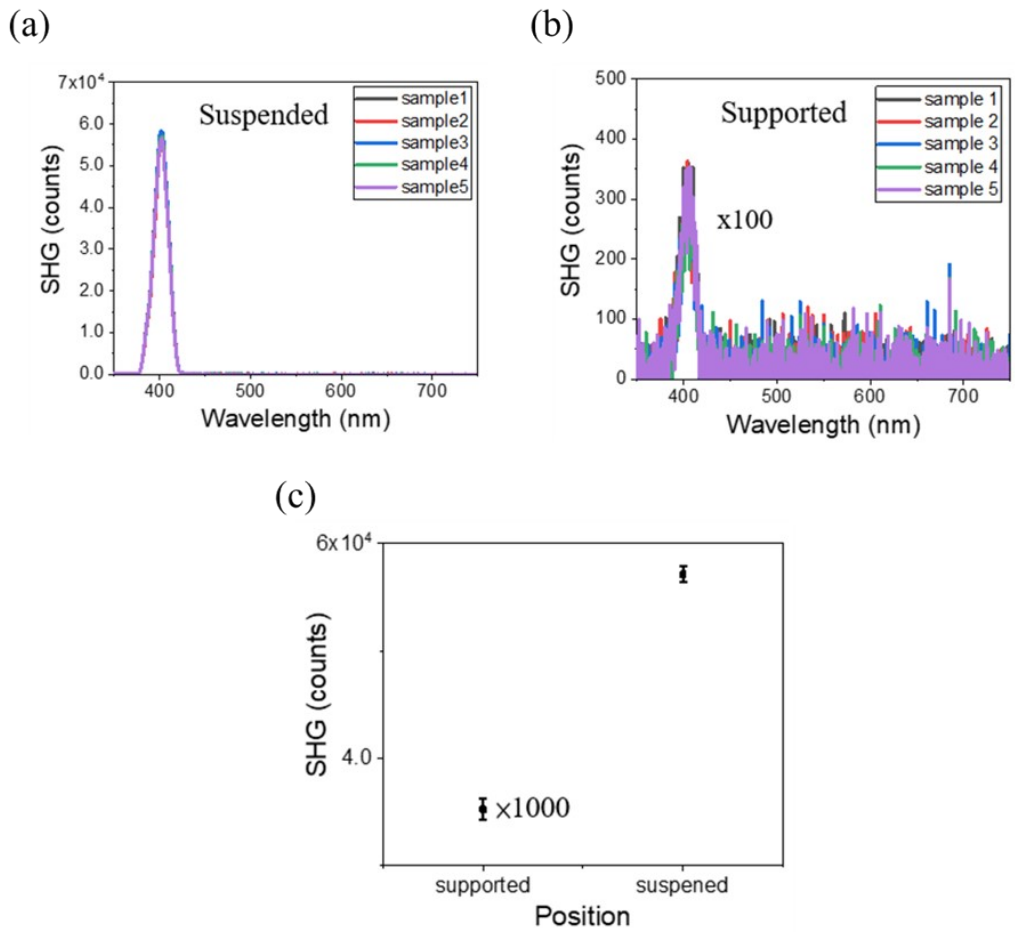

Figure S6 Averaged SHG spectra measured from (a) suspended and (b) supported MoS_2 for five independently prepared samples. (c) Statistical comparison of SHG intensities measured at supported and suspended regions (mean ± standard deviation, n = 25).

Supplementary Information Note S7. Power-dependent SHG signals

SHG signals excited by an 800 nm femtosecond (fs) laser are centered at approximately 400 nm. To further confirm that the peak near 400 nm originates from SHG, we employed various attenuators to investigate the relationship between excitation power and SHG intensity.

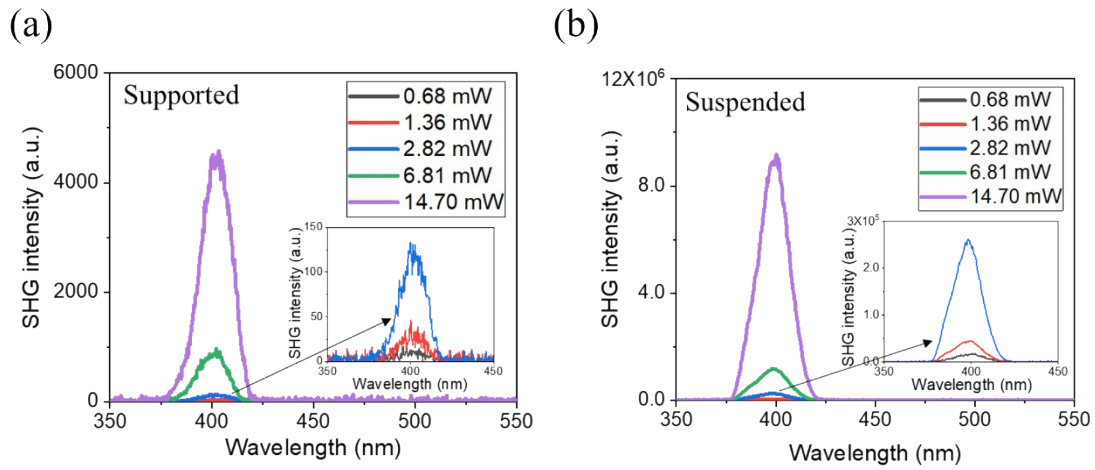

Figure S7. Power-dependent SHG spectra of (a) supported and (b) suspended MoS_2 flakes under the 800 nm fs laser excitation. The insets magnify the power-dependent SHG spectra for both (a) supported and (b) suspended MoS_2 flakes, with excitation power varying from 0.68 to 2.82 W.

Supplementary Information Note S8. Degree of SHG polarization anisotropy

Through polarization-resolved SHG measurements, the SHG signal intensities in the armchair and zigzag directions were obtained through fitting to evaluate the degree of SHG polarization anisotropy.

Table S3. SHG intensity and degree of SHG polarization anisotropy in MoS_2 under different laser treatment times.

Laser treatment times	**0 s**	**10 s**	**20 s**	**30 s**	**40 s**	**60 s**	**120 s**
$I_{armchair}$	949.7	905.7	879.3	841.9	746.5	503.0	341.5
I_{zigzag}	3.8	12.2	21.3	34.1	41.0	54.7	65.8
$\frac{I_{armchair} - I_{zigzag}}{I_{armchair} + I_{zigzag}}$	99.2%	97.3%	95.3%	92.2%	89.6%	80.4%	67.7%

Reference

1. Y.-C. Lee, Y.-C. Tseng and H.-L. Chen, *ACS Photonics*, 2017, **4**, 93-105.